The anharmonic quantum fluctuation of the stretching (bending) mode becomes more (less) pronounced as the H bond gets stronger (*9*), which accounts for the observed crossover behavior in region II. However, the reversal behaviors in regions I and III are not predicted by this simple theoretical picture. At the weak-bond limit (region I), the quantum contributions of these two modes both diminish quickly and tend to cancel each other, resulting in the fade-out of the energy difference. The turning point at the strong-bond limit (region III) is closely related to the unusual noncolinear geometry of the O–H···Cl H bond, which arises from the electric repulsive interaction between the H1 (D1) atom and the Na^+ cation of the NaCl surface (fig. S12). Such an interaction modifies the potential profile along the H-bond bending direction as the water molecule approaches the surface, so anharmonic H-bond bending is greatly enhanced and even dominates over O–H stretching, leading to the reversal behavior of NQEs for strong H bonds. This implies that the NQEs of a H bond are extremely sensitive to coupling with the local environment, which is, at present, inaccessible by macroscopic spectroscopic methods. Not only do these findings substantially advance our understanding of the quantum nature of H bonds, they also open up a new route for spectroscopic studies of H-bonded systems at the single-bond level.

REFERENCES AND NOTES

1. N. Greenwood, A. Earnshaw, *Chemistry of the Elements* (Butterworth Heinemann, 1997).
2. A. Hodgson, S. Haq, *Surf. Sci. Rep.* **64**, 381–451 (2009).
3. M. Benoit, D. Marx, M. Parrinello, *Nature* **392**, 258–261 (1998).
4. A. K. Soper, C. J. Benmore, *Phys. Rev. Lett.* **101**, 065502 (2008).
5. F. Paesani, G. A. Voth, *J. Phys. Chem. B* **113**, 5702–5719 (2009).
6. M. E. Tuckerman, D. Marx, M. L. Klein, M. Parrinello, *Science* **275**, 817–820 (1997).
7. G. A. Voth, D. Chandler, W. H. Miller, *J. Chem. Phys.* **91**, 7749–7760 (1989).
8. J. A. Morrone, R. Car, *Phys. Rev. Lett.* **101**, 017801 (2008).
9. X. Z. Li, B. Walker, A. Michaelides, *Proc. Natl. Acad. Sci. U.S.A.* **108**, 6369–6373 (2011).
10. D. F. Brougham, R. Caciuffo, A. J. Horsewill, *Nature* **397**, 241–243 (1999).
11. C. Andreani, D. Colognesi, J. Mayers, G. F. Reiter, R. Senesi, *Adv. Phys.* **54**, 377–469 (2005).
12. A. Pietropaolo *et al.*, *Phys. Rev. Lett.* **100**, 127802 (2008).
13. Y. Harada *et al.*, *Phys. Rev. Lett.* **111**, 193001 (2013).
14. Y. Nagata, R. E. Pool, E. H. G. Backus, M. Bonn, *Phys. Rev. Lett.* **109**, 226101 (2012).
15. B. C. Stipe, M. A. Rezaei, W. Ho, *Science* **280**, 1732–1735 (1998).
16. Y. Kim, T. Komeda, M. Kawai, *Phys. Rev. Lett.* **89**, 126104 (2002).
17. A. J. Heinrich, C. P. Lutz, J. A. Gupta, D. M. Eigler, *Science* **298**, 1381–1387 (2002).
18. H. Gawronski, M. Mehlhorn, K. Morgenstern, *Science* **319**, 930–933 (2008).
19. N. Lorente, M. Persson, *Phys. Rev. Lett.* **85**, 2997–3000 (2000).
20. M. Galperin, M. A. Ratner, A. Nitzan, A. Troisi, *Science* **319**, 1056–1060 (2008).
21. K. Morgenstern, J. Nieminen, *Phys. Rev. Lett.* **88**, 066102 (2002).
22. Supplementary materials are available on *Science* Online.
23. J. Guo *et al.*, *Nat. Mater.* **13**, 184–189 (2014).
24. B. N. J. Persson, A. Baratoff, *Phys. Rev. Lett.* **59**, 339–342 (1987).
25. M. Galperin, M. A. Ratner, A. Nitzan, *J. Chem. Phys.* **121**, 11965–11979 (2004).
26. H. Song *et al.*, *Nature* **462**, 1039–1043 (2009).
27. M. Rozenberg, A. Loewenschuss, Y. Marcus, *Phys. Chem. Chem. Phys.* **2**, 2699–2702 (2000).
28. T. Steiner, *Angew. Chem. Int. Ed.* **41**, 48–76 (2002).
29. N. Lorente, M. Persson, L. J. Lauhon, W. Ho, *Phys. Rev. Lett.* **86**, 2593–2596 (2001).
30. M. Ohara, Y. Kim, S. Yanagisawa, Y. Morikawa, M. Kawai, *Phys. Rev. Lett.* **100**, 136104 (2008).
31. C. L. Chiang, C. Xu, Z. Han, W. Ho, *Science* **344**, 885–888 (2014).
32. I. V. Stiopkin *et al.*, *Nature* **474**, 192–195 (2011).
33. A. V. Iogansen, *Spectrochim. Acta A* **55**, 1585–1612 (1999).
34. Y. Li *et al.*, *Nano Lett.* **16**, 1104–1109 (2016).

ACKNOWLEDGMENTS

This work was supported by the National Basic Research Programs of China under grant 2012CB921303 and the National Natural Science Foundation of China under grants 91321309, 11290162/A040106, 11304107, 61371015, 11422431, 11275008, 11274002, and 91021007. Y.J. acknowledges support from the National Program for Support of Top-Notch Young Professionals. We are grateful for the computational resources provided by the supercomputer TianHe-1A in Tianjin, China.

SUPPLEMENTARY MATERIALS

www.sciencemag.org/content/352/6283/321/suppl/DC1
Materials and Methods
Supplementary Text
Figs. S1 to S12
References (*35*–*50*)

6 January 2016; accepted 14 March 2016
10.1126/science.aaf2042

THERMODYNAMICS

A single-atom heat engine

Johannes Roßnagel,[1]* Samuel T. Dawkins,[1] Karl N. Tolazzi,[2] Obinna Abah,[3] Eric Lutz,[3] Ferdinand Schmidt-Kaler,[1] Kilian Singer[1,4]*

Heat engines convert thermal energy into mechanical work and generally involve a large number of particles. We report the experimental realization of a single-atom heat engine. An ion is confined in a linear Paul trap with tapered geometry and driven thermally by coupling it alternately to hot and cold reservoirs. The output power of the engine is used to drive a harmonic oscillation. From direct measurements of the ion dynamics, we were able to determine the thermodynamic cycles for various temperature differences of the reservoirs. We then used these cycles to evaluate the power P and efficiency η of the engine, obtaining values up to $P = 3.4 \times 10^{-22}$ joules per second and $\eta = 0.28\%$, consistent with analytical estimations. Our results demonstrate that thermal machines can be reduced to the limit of single atoms.

Heat engines, which convert thermal energy into mechanical work, have played a central role in society since the industrial revolution and are ubiquitous as generators of motion (*1*). The working fluid of a macroscopic engine typically contains on the order of 10^{24} particles. Experimental progress in the past decade has led to the miniaturization of thermal machines down to the microscale, using microelectromechanical (*2*), piezoresistive (*3*), and cold atom (*4*) systems, as well as single colloidal particles (*5*, *6*) and single molecules (*7*). In his 1959 talk "There is plenty of room at the bottom," Feynman envisioned tiny motors working at the single-atom level (*8*).

Here, we report the realization of a classical single-atom heat engine whose working agent is an ion held within a modified linear Paul trap. We use laser cooling and electric-field noise to engineer cold and hot reservoirs. To determine the temperature of the ion, we make use of fast thermometry methods, which make use of the Doppler broadening of optical resonances (*9*). The thermodynamic cycle of the engine is established for various temperature differences of the reservoirs, from which we deduce work and heat, and thus power output and efficiency. We additionally show that the work produced by the engine can be effectively stored and used to drive a harmonic oscillator against friction.

Trapped ions offer an exceptional degree of control in their preparation and manipulation, great precision in the measurement of their parameters (*10*, *11*), and the capability of coupling to engineered reservoirs (*12*, *13*). Hence, they provide an ideal setup for operating and characterizing a single-particle heat engine (*14*).

In our experiment, a single $^{40}Ca^+$ ion is trapped in a linear Paul trap with a funnel-shaped electrode geometry (Fig. 1A). The electrodes are driven symmetrically at a radio-frequency voltage of 830 V_{pp} at 21 MHz, resulting in a tapered harmonic pseudo-potential (Fig. 1B) of the form $U = (m/2)\sum_i \omega_i^2 i^2$ (*10*), where m is the atomic mass and $i \in \{x, y\}$ denotes the radial trap axes (Fig. 1A). The axial confinement is realized with constant voltages on the two end-cap electrodes, resulting in a trap frequency of $\omega_z/2\pi = 81$ kHz. The trap angle $\theta = 10°$ and the radial extent of the trap $r_0 = 1.1$ mm at $z = 0$ characterize the geometry of the funnel. The resulting radial trap frequencies $\omega_{x,y}$ decrease in the axial z-direction as

$$\omega_{x,y} = \frac{\omega_{0x,0y}}{\left(1 + \frac{z \tan\theta}{r_0}\right)^2} \quad (1)$$

The eigenfrequencies in the radial directions at the

[1]QUANTUM, Institut für Physik, Universität Mainz, D-55128 Mainz, Germany. [2]Max-Planck-Institut für Quantenoptik, D-85748 Garching, Germany. [3]Department of Physics, Friedrich-Alexander-Universität Erlangen-Nürnberg, D-91058 Erlangen, Germany. [4]Experimentalphysik I, Universität Kassel, D-34132 Kassel, Germany.
*Corresponding author. E-mail: j.rossnagel@uni-mainz.de (J.R.); ks@uni-kassel.de (K.S.)

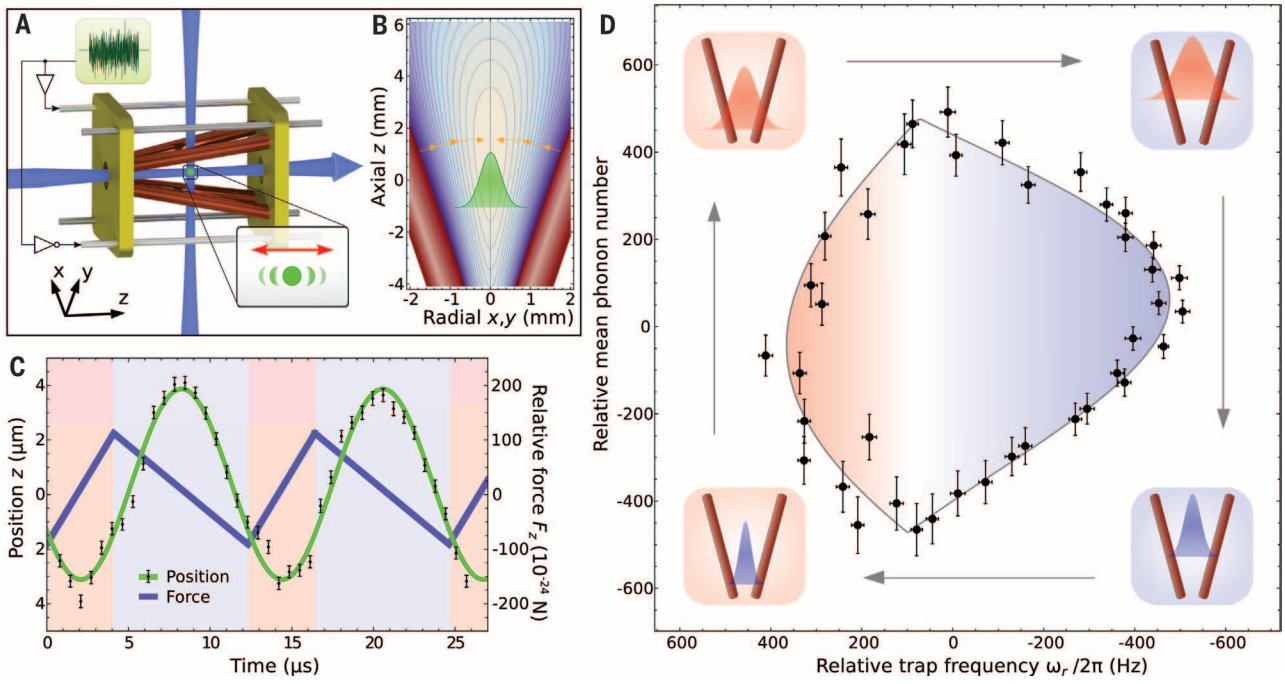

Fig. 1. Single-atom heat engine. (**A**) Experimental setup composed of a single trapped ion (green); lasers for cooling, damping, and observation of the ion (blue); radio-frequency electrodes in funnel geometry (red); end caps (gold); and outer electrodes (gray). The position of the ion is imaged on an ICCD camera. Opposing voltage noise waveforms are additionally supplied to the outer electrodes so as to generate electric-field noise without affecting the trap frequencies. (**B**) Cross section of the funnel-shaped pseudo-potential between the radio-frequency electrodes (red), with a minimum at the center. The gradient of the potential (orange arrows) has an axial component that increases with radial displacement x or y. A force in the axial direction arises as a function of the finite width of the radial thermal state of the ion (green Gaussian distribution). (**C**) Position of the ion (black symbols) determined from the average of more than 200,000 camera images at each time step. The error bars result from the uncertainty of Gaussian fits to the recorded fluorescence images. The measured positions are described by a sinusoidal fit (green line). Background colors indicate the periodic interaction with the hot (red) and cold (blue) reservoirs, which gives rise to a periodic driving force (blue line) according to Eq. 1, shown relative to its mean value of 5.03×10^{-21} N. (**D**) Thermodynamic cycle of the engine for one radial direction. Trap frequencies in the radial direction ω_r are deduced directly from the measured z-positions. The temperature T of the radial state of motion, and thus the corresponding mean phonon number $\overline{n}_r$, is determined from separate measurements (see text and Fig. 2). The values of ω_r and $\overline{n}_r$ are given with respect to the center of the cycle at $\omega_{0r}/2\pi = 447.9 \pm 0.2$ kHz and $\overline{n}_{0r} = 2.61\ (\pm 0.04) \times 10^4$ phonons. The shaded area enclosed by the cycle is proportional to the work performed by the engine, where red and blue colors indicate heating and cooling periods, respectively. The black line is the calculated trajectory of the cycle (see text). The pictograms in the corners illustrate the different stages of an idealized cycle.

trap minimum $z = 0$ are $\omega_{0x}/2\pi = 447$ kHz and $\omega_{0y}/2\pi = 450$ kHz, with the degeneracy lifted, but sufficiently close to permit the approximation of cylindrical symmetry with $r^2 = x^2 + y^2$ and a mean radial trap frequency ω_r. An additional set of outer electrodes compensates for stray fields. The trapped ion is cooled by a laser beam at 397 nm, which is red-detuned to the internal electronic $S_{1/2} - P_{1/2}$ transition (*10*); the resulting fluorescence is recorded by a rapidly gated intensified charge-coupled device (ICCD) camera.

The heating and cooling cycle of the ion is designed such that the ion thermalizes as if in contact with a thermal reservoir. A cold bath interaction is realized by exposing the ion to a laser cooling beam, leading to an equilibrium temperature of $T_C = 3.4$ mK (*9*, *15*). A hot reservoir interaction with finite temperature T_H is designed by additionally exposing the ion to white electric-field noise. The interplay of photon scattering and noise leads to a thermal state of the ion at temperature T at any given moment (*9*, *16*, *17*).

In our setup, heating and cooling act on the radial degrees of freedom. The resulting time-averaged spatial distribution of the radial thermal state is of the form

$$\xi_r(r, \phi, T) = \frac{1}{2\pi\sigma_r^2(T)} \exp\left[\frac{-(r - r_0)^2}{2\sigma_r^2(T)}\right] \quad (2)$$

with a temperature-dependent time-averaged width $\sigma_r(T) = \sqrt{k_B T/m\omega_r^2}$, where k_B is the Boltzmann constant. Because the thermal energy during the operation of the engine is larger than the energy spacing of the harmonic oscillator ($k_B T >> \hbar\omega_r$), a classical description of the dynamics is appropriate.

The heat engine is driven by alternately heating and cooling the ion in the radial direction by switching the electric noise on and off; the cooling laser is always on. Heating and cooling change the spatial width $\sigma_r(T)$ of the radial thermal state $\xi_r(r, \phi, T)$. Owing to the geometry of the trap, the gradient of the funnel-shaped pseudo-potential U has a component in the axial direction z that depends on the radial position r (Fig. 1B). As a consequence, the finite width of the radial thermal state $\xi_r(r, \phi, T)$ leads to a temperature-dependent average force in the axial direction:

$$F_z(T) = -\int_0^{2\pi}\int_0^{\infty} \xi_r(r, \phi, T) \frac{dU(r)}{dz} r\, dr\, d\phi \quad (3)$$

During the first part of the cycle, the ion is heated and the width $\sigma_r(T)$ increases. As a result, the ion moves along the z axis to a weaker radial confinement. We calculate a static displacement of 11 nm for the relative change of $\Delta F_z = 2 \times 10^{-22}$ N, corresponding to Fig. 1C. During this first step, the axial potential energy of the ion increases and work is produced. The second step occurs during exposure to the cold reservoir when the electric-field noise is switched off. Here the radial width σ_r and the corresponding force F_z decrease as the temperature is reduced, and the ion moves back to its initial position owing to the restoring force of the axial potential. The combination of heating and cooling gives rise to a closed thermodynamic cycle and leads to a periodic force $F_z(T)$ in the axial direction (Fig. 1C). We switch between heating and cooling with precise timing, such

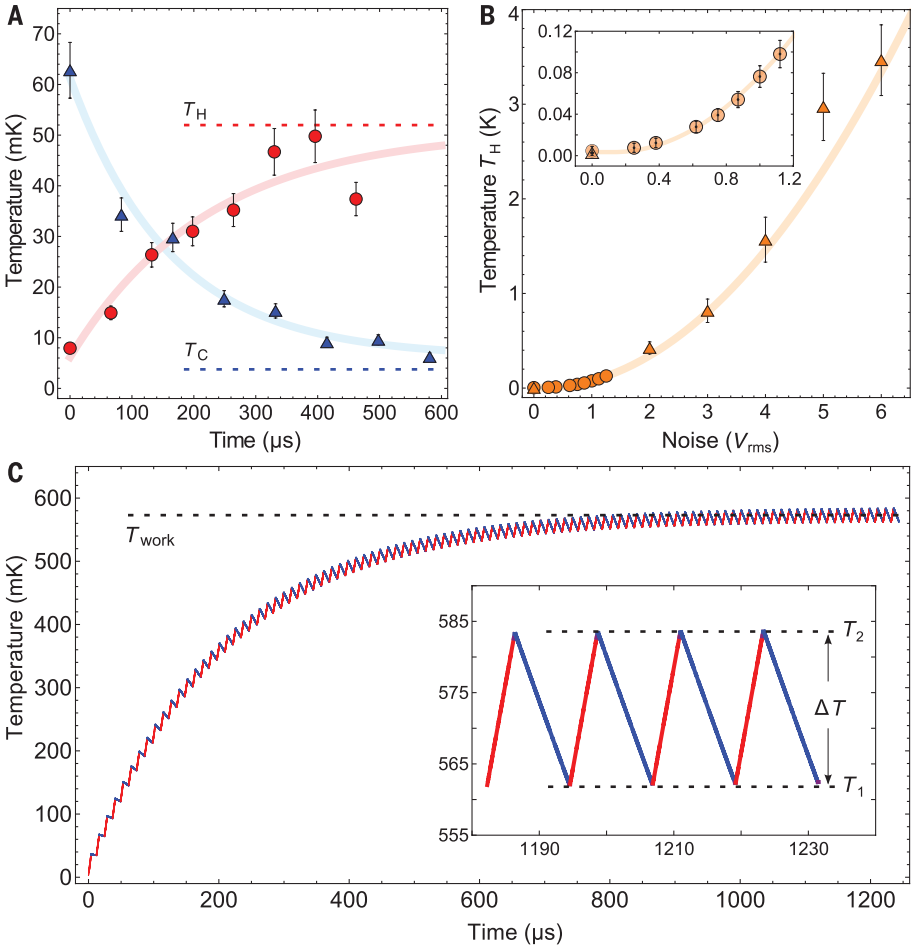

Fig. 2. Temperature dynamics of the engine. (**A**) Thermalization curves derived from dark-state thermometry of the radial thermal state of the ion when heated to T_H = 51 mK (red) and cooled to T_C = 6 mK (blue). Individual errors result from fits to the dark resonances as well as the uncertainty caused by the laser linewidths (*9*). Individual fits reveal thermalization time constants for heating and cooling of t_H = 190 ± 30 μs and t_C = 210 ± 10 μs, respectively. (**B**) Dependence of the hot bath temperature T_H on the root mean square of the electric noise applied to the trap electrodes, measured by dark-state thermometry (circles) (*9*) and spatial thermometry (triangles) (*21*). The inset shows a magnification of the low-temperature values. (**C**) Simulated temperature of the ion as a function of time using the parameters for thermalization. Heating and cooling durations in each cycle are 4.1 μs and 8.2 μs, respectively. With an electric-field noise amplitude of 4 V, we calculate a working point temperature T_{work} = 568 mK and a temperature difference $\Delta T = T_2 - T_1$ = 21.5 mK. The inset shows an enlargement of the cooling and heating processes at steady-state operation.

that the cycle repeats itself at a rate equal to the axial trap frequency ω_z. The engine therefore effectively drives a harmonic oscillation in the axial direction. The work produced in each cycle is thus resonantly transferred to the axial degree of freedom and stored in the amplitude of the oscillation. The essentially frictionless nature of the system leads to an ever-increasing oscillation. The axial motion thus plays a role similar to the flywheel of a mechanical engine.

To contain this oscillation, we provide adjustable damping by introducing an additional cooling laser in the axial direction. Steady-state operation is reached when the work generated by the engine is balanced by the energy dissipated by the damping. We measure the amplitude of the steady-state oscillation of the ion in the *z*-direction by recording fluorescence images with the ICCD camera; the exposure time is 700 ns, which is much shorter than the axial oscillation period. The camera is synchronized with the temperature modulation, allowing for the repetitive recording of images at particular phases of the oscillation. Thus, the position of the ion can be determined precisely as a function of time, thereby revealing the amplitude and phase of the resulting sinusoidal oscillation (*18*) (Fig. 1C). We verified that both are independent to an inversion of the noise signal. To facilitate the position measurement, we use the damping laser to reduce the incoherent, thermal motion in the axial direction, which originates from bath interactions. For efficient cooling while maintaining low damping of the oscillation, the laser is applied only around the turning points of the axial motion (*15*).

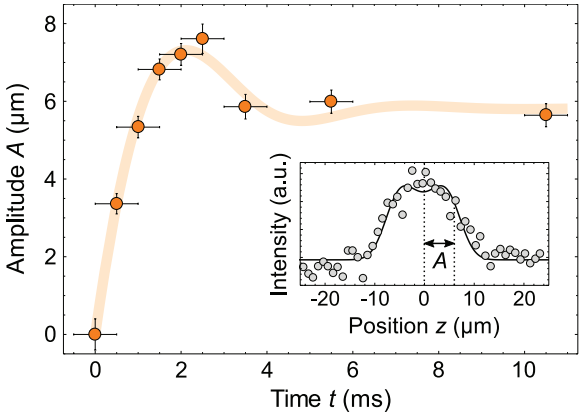

Fig. 3. Determination of the damping coefficient. The effect of the damping coefficient γ is studied by directly driving the ion axially with the end caps in the absence of the thermal reservoir interactions. The step response is observed by determining the amplitude A of the ion's oscillation (orange circles) at time t after switching the end cap drive on. In accord with the dynamics of a driven damped harmonic oscillator, the step response features a rise toward a steady-state amplitude A_0, superposed with a decaying beat frequency at ω_b between the resonance ω_z and drive frequency ω_d according to the relation $A(t) = A_0\sqrt{[\cos(\omega_b t) - (\omega_z/\omega_d)\exp(-\gamma_i t)]^2 + \sin(\omega_b t)^2}$. A fit to the data (orange line) reveals γ_i = 560 ± 100 s^{-1}; the average of four such measurements yielded γ = 480 ± 140 s^{-1}. (**Inset**) Determination of oscillation amplitude at 5.5 ms by fitting a time-integrated sinusoidally modulated Gaussian (black line) to the projections of the corresponding camera images, with exposure time of 1 ms (gray circles). The width of the Gaussian is determined from the image of an ion at rest.

The thermodynamic cycle of the single-ion heat engine is shown in Fig. 1D by plotting the

mean phonon number $\bar{n}_r = k_B T/\hbar\omega_r$ of the thermal state of the ion in the radial direction as a function of the corresponding trap frequency ω_r (*19*). The radial trap frequencies $\omega_r(t)$ are obtained from the measured axial positions of the ion $z(t)$ in conjunction with calibration measurements of the tapered confinement described by Eq. 1. The temperature of the ion at any given moment of the cycle is deduced from the interplay of the heating and cooling rates (Fig. 2). We determine these rates via a stroboscopic measurement of the thermal broadening of narrow resonances of dark states caused by coherent population trapping, which are sensitive to the velocity of the ion through the Doppler shift (Fig. 2A). A detailed description of this technique, originally used for cold atoms (*20*), is presented in (*9*). The temperature of the hot reservoir T_H can be adjusted via the applied electric-field noise and has been measured using dark-state thermometry, as well as spatial thermometry (*21*) for higher temperatures (Fig. 2B). The heating and cooling processes are much slower than the internal dynamics of the ion; thus, the cycle can be regarded as quasi-static with negligible losses caused by irreversible processes (*22*). Because the ion is in permanent contact with one of the reservoirs, the dynamics are similar to those of a Stirling engine (*5*, *23*).

We derived the power output during steady-state operation in three independent ways. We first determined the power $P_{cyc} = W_{cyc}/t_{cyc}$, with cycle time $t_{cyc} = 2\pi/\omega_z$, by evaluating the work as the area of the cycles for both radial directions, $W_{cyc} = \hbar \oint 2\bar{n}_r d\omega_r$ (*19*). To assess the performance of the engine, we computed the power for various temperature differences $\Delta T = T_2 - T_1$ between maximum temperature T_2 and minimum temperature T_1 in the cycle, as defined in Fig. 2C. The difference ΔT can be tuned by adjusting either the reservoir temperatures or the relative duration of the reservoir interaction, given by the duty cycle $d = t_H/t_{cyc}$ of the hot bath interaction time t_H per cycle.

We alternatively deduced the power directly from the measurement of the axial oscillation amplitudes A_z of up to 15 μm. The driving power of a driven damped harmonic oscillator at steady state yields $P_{osc} = \gamma m \omega_z^2 A_z^2$ (*24*). The damping parameter $\gamma = 480 \pm 140\ s^{-1}$ was determined separately via observation of the step response of the ion's oscillation to a coherent drive (Fig. 3). Both methods give consistent values of the power, of up to $3.4\ (\pm 0.5) \times 10^{-22}$ J/s, depending on ΔT (Fig. 4A). This represents a power-to-particle ratio of 1.5 kW/kg, comparable to that of a typical car engine, indicating that the power scales approximately with the number of particles of the working agent.

We further calculated analytically the engine output power using the expression for work performed during a single cycle:

$$W_{ana} = -\oint F_z(t)\frac{dz(t)}{dt}dt \qquad (4)$$

The driving force F_z is calculated from Eq. 3, accounting for the temperature variations of the ion determined as shown in Fig. 2C and neglecting the weak z dependence. The resulting motion $z(t)$ is derived assuming expressions of a resonantly driven damped harmonic oscillator. Thus, for the output power, we find

$$P_{ana} = \frac{W_{ana}}{t_{cyc}} = \frac{4k_B^2 \sin^2(\pi d)\tan^2\theta\,\Delta T^2}{m\pi^4\gamma[(d^2-d)r_0]^2}$$

$$= (8.8 \times 10^{-20}\ \mathrm{Js^{-1}K^{-2}})\Delta T^2 \qquad (5)$$

This analytical formula is plotted using experimental parameters in Fig. 4A and is in agreement with the measured P_{cyc}.

We further evaluated the efficiency of the engine, $\eta_{cyc} = W_{cyc}/Q_H$, from the measured data by determining the heat absorbed from the hot reservoir, $Q_H = \int_H T dS$, from the TS diagram shown in Fig. 4B. Here, S denotes the entropy of a thermal harmonic oscillator, $S = k_B[1 + \ln(k_B T/\hbar\omega_r)]$ (*22*, *25*). To this end, we transformed the measured data of the cycle in Fig. 2B according to $\{\omega_r, \bar{n}_r\} \rightarrow \{S, T\}$. Using the above analytical approach, we find

$$\eta_{ana} = \frac{4k_B \sin^2(\pi d)\tan^2\theta\,\Delta T}{m\pi^3\gamma\omega_z[(d^2-d)r_0]^2} = (0.041\mathrm{K}^{-1})\Delta T \qquad (6)$$

The resulting efficiencies (Fig. 4C) reach values up to $\eta_{cyc} = 0.28 \pm 0.07\%$, in agreement with the analytical expectation. A comparison of this value with the corresponding efficiency at maximum

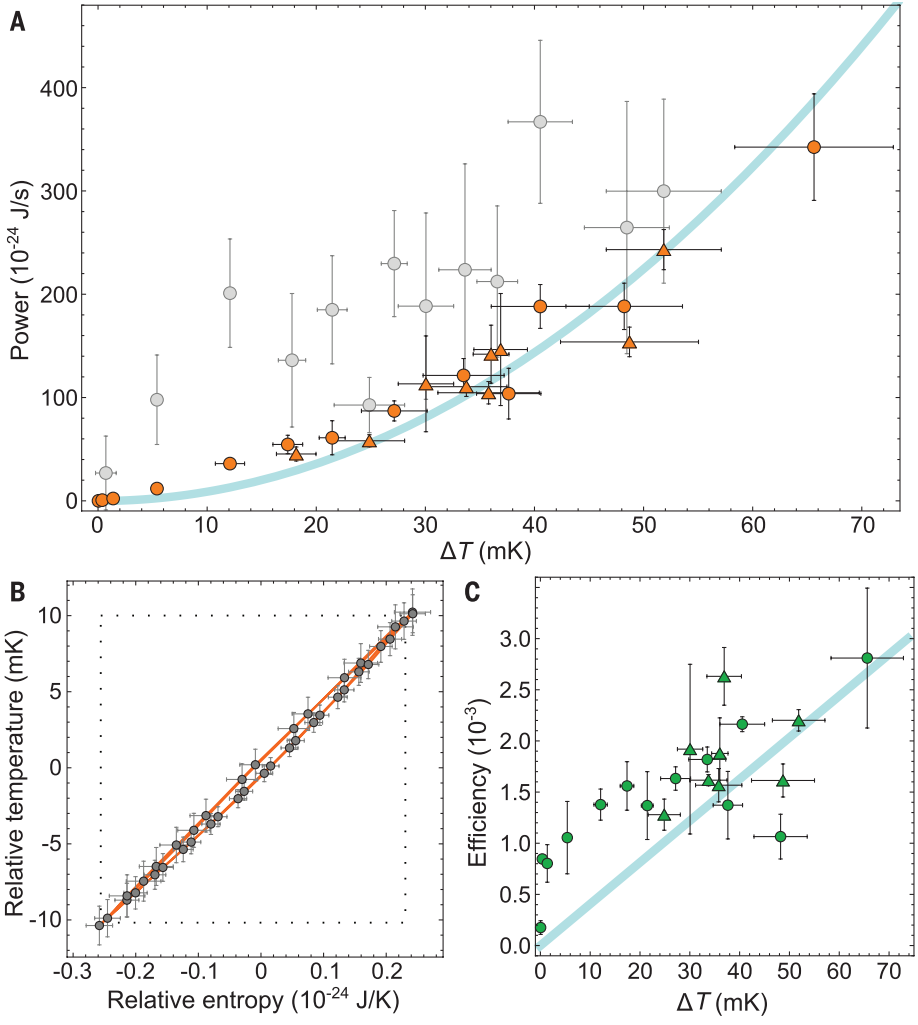

Fig. 4. Power and efficiency of the heat engine. (**A**) Power of the engine, calculated from the measured cycles (orange) and from a direct analysis of the amplitude (gray). The temperature differences ΔT were achieved by varying the electric-field noise (circles) and the duty cycle of heating and cooling (triangles). The measured cycle data are consistent with the expected value from analytical calculations (blue line). The larger error bars of the gray data stem from the uncertainty on the damping coefficient γ. (**B**) The heat engine cycle, corresponding to Fig. 1D; temperature is shown relative to 568 mK and entropy relative to 179.6×10^{-24} J/K. Both work and efficiency can be derived from integrating this cycle. The square (dotted line) represents the equivalent Carnot cycle for the full range of parameters and shows the case of the theoretical maximum efficiency. (**C**) Measured efficiency as a function of ΔT, which was tuned by varying the noise amplitude (circles) or the duty cycle (triangles), compared to the result of the analytical calculation (blue line).

power, given by the Curzon-Ahlborn (*26*) formula $\eta_{CA} = 1 - \sqrt{T_1/T_2} = 1.9\%$, reflects that the current trap parameters do not correspond to the optimal point (*14*). The performance of future single-ion heat engines could be improved by redesigning the geometry of the trap to have cycles with a higher range of frequencies ω_r (see Fig. 4B). This could be achieved by increasing either the angle of the taper or the absolute radial trap frequencies.

We have demonstrated a realization of a heat engine whose working agent is a single atom. This classical device offers a broad platform for future experiments investigating, for instance, machines coupled to nonthermal reservoirs (*27*) or single-ion refrigerators and pumps (*28*). Moreover, the quantum regime ($k_B T \approx \hbar\omega_r$) could be reached by replacing Doppler cooling by electromagnetically induced transparency cooling or side-band cooling (*10*), as in the recent verification of the quantum Jarzynski equality (*29*). In the quantum domain, dark-state thermometry could be replaced by side-band spectroscopy, again allowing for the determination of the cycle of the engine and thus its power and efficiency. Such a system would permit the study of the performance of small quantum machines (*30*, *31*) and the exploration of genuine quantum effects in thermodynamics, such as quantum coherences (*32*) and correlations (*33*), as well as the testing of predictions of quantum resource theory (*34*, *35*).

REFERENCES AND NOTES

1. Y. A. Çengel, M. A. Boles, M. Kanoğlu, *Thermodynamics: An Engineering Approach* (McGraw-Hill, ed. 8, 2014).
2. S. Whalen, M. Thompson, D. Bahr, C. Richards, R. Richards, *Sens. Actuators A* **104**, 290–298 (2003).
3. P. Steeneken *et al.*, *Nat. Phys.* **7**, 354–359 (2011).
4. J.-P. Brantut *et al.*, *Science* **342**, 713–715 (2013).
5. V. Blickle, C. Bechinger, *Nat. Phys.* **8**, 143–146 (2012).
6. I. A. Martínez *et al.*, *Nat. Phys.* **12**, 67–70 (2016).
7. T. Hugel *et al.*, *Science* **296**, 1103–1106 (2002).
8. R. P. Feynman, *Eng. Sci.* **23**, 22 (1960).
9. J. Roßnagel, K. N. Tolazzi, F. Schmidt-Kaler, K. Singer, *New J. Phys.* **17**, 045004 (2015).
10. D. Leibfried, R. Blatt, C. Monroe, D. Wineland, *Rev. Mod. Phys.* **75**, 281–324 (2003).
11. R. Blatt, D. Wineland, *Nature* **453**, 1008–1015 (2008).
12. J. F. Poyatos, J. I. Cirac, P. Zoller, *Phys. Rev. Lett.* **77**, 4728–4731 (1996).
13. C. J. Myatt *et al.*, *Nature* **403**, 269–273 (2000).
14. O. Abah *et al.*, *Phys. Rev. Lett.* **109**, 203006 (2012).
15. H. J. Metcalf, P. van der Straten, *Laser Cooling and Trapping* (Springer, 1999).
16. J. I. Cirac, R. Blatt, P. Zoller, W. D. Phillips, *Phys. Rev. A* **46**, 2668–2681 (1992).
17. J. I. Cirac, M. Lewenstein, P. Zoller, *Phys. Rev. Lett.* **72**, 2977–2980 (1994).
18. H. C. Nägerl, D. Leibfried, F. Schmidt-Kaler, J. Eschner, R. Blatt, *Opt. Express* **3**, 89–96 (1998).
19. B. Lin, J. Chen, *Phys. Rev. E* **67**, 046105 (2003).
20. T. Peters, B. Wittrock, F. Blatt, T. Halfmann, L. P. Yatsenko, *Phys. Rev. A* **85**, 063416 (2012).
21. S. Knünz *et al.*, *Phys. Rev. A* **85**, 023427 (2012).
22. G. S. Agarwal, S. Chaturvedi, *Phys. Rev. E* **88**, 012130 (2013).
23. K. Brandner, K. Saito, U. Seifert, *Phys. Rev. X* **5**, 031019 (2015).
24. J. R. Taylor, *Classical Mechanics* (University Science, Sausalito, CA, 2005).
25. L. D. Landau, E. M. Lifschitz, *Statistical Physics* (Elsevier, 1980).
26. F. Curzon, B. Ahlborn, *Am. J. Phys.* **43**, 22 (1975).
27. J. Roßnagel, O. Abah, F. Schmidt-Kaler, K. Singer, E. Lutz, *Phys. Rev. Lett.* **112**, 030602 (2014).
28. B. Lin, J. Chen, *Phys. Rev. E* **68**, 056117 (2003).
29. S. An *et al.*, *Nat. Phys.* **11**, 193–199 (2014).
30. N. Linden, S. Popescu, P. Skrzypczyk, *Phys. Rev. Lett.* **105**, 130401 (2010).
31. R. Kosloff, A. Levy, *Annu. Rev. Phys. Chem.* **65**, 365–393 (2014).
32. M. O. Scully, M. S. Zubairy, G. S. Agarwal, H. Walther, *Science* **299**, 862–864 (2003).
33. R. Dillenschneider, E. Lutz, *Europhys. Lett.* **88**, 50003 (2009).
34. F. G. Brandão, M. Horodecki, J. Oppenheim, J. M. Renes, R. W. Spekkens, *Phys. Rev. Lett.* **111**, 250404 (2013).
35. M. Horodecki, J. Oppenheim, *Nat. Commun.* **4**, 2059 (2013).

ACKNOWLEDGMENTS

We thank Princeton Instruments for the loan of the ICCD camera and S. Deffner for fruitful discussions. Supported by the German Research Foundation (grant "Einzelionenwärmekraftmaschine"), the Volkswagen Foundation (grant "Atomic Nano-Assembler"), European Union (EU) COST action MP1209, and the EU Collaborative Project TherMiQ (grant agreement 618074). The data presented in this report are available upon request to K.S.

14 October 2015; accepted 4 March 2016
10.1126/science.aad6320

ORGANOMETALLICS

Pre-transmetalation intermediates in the Suzuki-Miyaura reaction revealed: The missing link

Andy A. Thomas and Scott E. Denmark*

Despite the widespread application of Suzuki-Miyaura cross-coupling to forge carbon-carbon bonds, the structure of the reactive intermediates underlying the key transmetalation step from the boron reagent to the palladium catalyst remains uncertain. Here we report the use of low-temperature rapid injection nuclear magnetic resonance spectroscopy and kinetic studies to generate, observe, and characterize these previously elusive complexes. Specifically, this work establishes the identity of three different species containing palladium-oxygen-boron linkages, a tricoordinate boronic acid complex, and two tetracoordinate boronate complexes with 2:1 and 1:1 stoichiometry with respect to palladium. All of these species transfer their boron-bearing aryl groups to a coordinatively unsaturated palladium center in the critical transmetalation event.

Palladium-catalyzed cross-coupling reactions have fundamentally changed the practice of organic synthesis. These reactions forge carbon-carbon bonds through the migration of a carbon-based substituent from a main group element to palladium, as exemplified by the Kumada-Tamao-Corriu (Mg) (*1*), Suzuki-Miyaura (B) (*2*), Stille-Migita-Kosugi (Sn) (*3*), Negishi (Zn) (*4*), and Hiyama-Denmark (Si) (*5*) reactions. The Nobel Prize–sharing Suzuki-Miyaura reaction (*6*) is currently the premier cross-coupling process and has been widely applied in organic (*7*), medicinal (*8*), and materials (*9*) chemistry. It is also frequently used in the industrial syntheses of fine chemicals (*10*) and pharmaceuticals (*11*) because of its demonstrated reliability, its functional group compatibility, and the low cost and ease of handling of a wide variety of commercially available boron-based reagents.

Despite the preeminent status of the Suzuki-Miyaura reaction, a fundamental understanding of the critical migratory transmetalation event from boron to palladium has thus far been lacking (*12*–*18*). For decades, chemists have considered two pathways (path A and path B in Fig. 1) that differ in the role that the hydroxide ion plays in initiating the transmetalation event. Path A proceeds through the combination of a negatively charged aryltrihydroxyboronate (compound **1**) and a palladium halide complex (**2**), which form a hypothetical intermediate containing a Pd-O-B unit (**3**). The alternative path B proceeds through the combination of a neutral arylboronic acid (**4**) and a palladium hydroxide complex (formed through the displacement of the organopalladium halide by hydroxide; **5**), ultimately converging to the same intermediate **3**, which is then poised to transfer the aryl group to palladium in an intramolecular β-aryl elimination step, followed by reductive elimination (Fig. 1). Species such as **3** represent the missing link between the starting organoboron reagents and the diorganopalladium intermediates that are known to afford cross-coupling products.

The role of the base in the Suzuki-Miyaura reaction was investigated initially by the Soderquist laboratory (*12*) and, more recently, by the laboratories of Hartwig (*13*), Amatore and Jutand (*14*–*16*), and Schmidt (*17*, *18*). The kinetic analysis in (*13*) established that path B is favored over path A by more than four orders of magnitude, a conclusion that is reinforced by the extensive kinetic studies in (*14*–*16*), which clearly identified multiple antagonistic roles for the hydroxide ion. Although nuclear magnetic resonance (NMR) spectroscopic and kinetic studies have

Roger Adams Laboratory, Department of Chemistry, University of Illinois, Urbana, IL 61801, USA.
***Corresponding author. E-mail: sdenmark@illinois.edu**